Deep ultraviolet-excited fluorescence histology with fibre optic illumination for tissue microtopography and quantitative mapping

Alexander Si Kai Yong*[1], Ko Hui Tan*[1], Joel Lang Yi Ang*[1,3],
Chiyo Wan Xuan Tan[4], Jessica Sze Jia Kng[4], Cyrus Jia Jun Tan[4], Rachael Hui Kie Soh[4],
Kaicheng Liang[1,2,3,5]

[1]Institute of Molecular and Cell Biology, [2]Institute of Microelectronics,
[3]Bioinformatics Institute, [4]Institute of Bioengineering and Bioimaging,
Agency for Science, Technology and Research (A*STAR), Singapore

[5]Lee Kong Chian School of Medicine, Nanyang Technological University (NTU), Singapore

*These authors contributed equally to this work

May 2023

Abstract

Cellular imaging of thick samples usually requires either physical sectioning or laser scanning microscopy, which are time-consuming and involved. We developed a compact fibre optic-illuminated imaging platform based on microscopy with ultraviolet (UV) surface excitation (MUSE) for cellular visualisation of thick sample surfaces. Optical fibres delivered illumination at steep oblique angles, optimising optical sectioning by minimising UV penetration depth, and enabled short-working-distance objective lenses. Multi-scale image mapping spanned single cells to murine organ slices of 8x12 mm and 1.3 million cells per surface. Omni-directional control of optical fibre illumination produced 3D microtopography, a new concept relevant to microstructure and heterogeneity studies. We demonstrated histological imaging validated against standard H&E, multiplexed fluorescence for protein expression, and quantitative mapping of cell and organ-scale viability including an analysis of antibiotic insult on *ex vivo* murine kidneys ($n = 12$). This technology addresses long-standing gaps in laboratories for visualising thick samples for near-real-time cellular insights.

1 Introduction

Comprehensive spatial insights from tissue and organs at the 'mesoscopic' centimetre-scale are of growing interest. Fluorescence imaging of large unsectioned samples is a key enabler in protein expression studies[1] and organ-level spatial transcriptomics[2]. Confocal[3], multiphoton microscopy[4], and light-sheet microscopy with tissue clearing[5] are the important techniques today but are costly and complex commercial offerings, usually available as shared infrastructure in privileged scientific organisations. An uncomplicated and economical microscope for rapid cellular imaging of thick, large samples could potentially scale to every lab bench, biotechnology outfit, and less-privileged hospital. This concept has been a long-standing challenge in surgical pathology[6] and is emerging in life science with stringent requirements on quantitative imaging, molecular specificity, and compatibility with laboratory assays[7]. Specifically for tissue, a fast analogue to conventional hematoxylin and eosin (H&E) histology is needed for thick or intact samples[8]. Label-free microscopy of biological samples based on optical coherence tomography[9, 10] or quantitative phase imaging[11] is attractive for their simplicity in sample preparation, but the lack of molecular multi-colour contrast hampers image interpretation.

The use of deep ultraviolet (DUV) illumination for fluorescence excitation is a recent promising approach for thick sample microscopy. DUV light penetrates unsectioned tissue superficially, providing optical sectioning, and can simultaneously excite multiple fluorophores using a single wavelength[12, 13]. Also known as microscopy

with ultraviolet surface excitation (MUSE), this technique's simplicity has been previously highlighted for its potential in intra-operative imaging[14, 15], although demonstrations in life science have been limited[16, 17]. Previous MUSE designs typically delivered DUV illumination directly from light-emitting diodes (LEDs) at an oblique angle. These designs required specialised long-working-distance objective lenses, adding to cost and size.

We propose a new illumination strategy, enabling advances in directional and DUV exposure control, light source management, objective lens selection, and 3D visualisation. We used multiple optical fibres on a custom 3D-printed angle-adjustable mount for omni-directional DUV illumination. This provided oblique light delivery at a short working distance and near-horizontal angle ($\sim$1 mm and $\sim$ 85° for 10X objective), minimising DUV penetration and enhancing optical sectioning. The fibre illumination also enabled micro-scale 3D topographic mapping using the photometric stereo algorithm[18]. Illumination was synchronised (only to turn on) with camera exposure. Our 30x30 cm platform used stepper motors with precision stages for stitching (mosaicing) image maps of samples up to 1.5 cm^2 in size. Large slices of murine organs up to 7.8 x 12.4 mm in size with $\sim$1.3 million cells could be imaged at cellular resolution. We developed 2-colour tissue staining protocols as an analogue to H&E histology, and protein expression visualisation using multiplexed immunohistochemical fluorescence. We further demonstrated our microscope as a powerful quantitative tool for studying the effects of an antibiotic drug insult on kidney viability.

2 Results

2.1 Fibre optic illumination

Multi-mode fibres coupled to DUV LEDs illuminated the sample from four directions (Fig. 1a, Supp. Fig. S1). Fibre optic illumination is an approach distinct from previous DUV microscope designs that typically had LEDs pointed directly at the sample (some with light guides or lensing), requiring a large space clearance afforded by long-working-distance objectives[19]. Biological samples were illuminated by four multi-mode fibres coupled either in pairs to two DUV LEDs (Fig. 1a, Supp. Fig. S1), or individually to separate LEDs for microtopography (Fig. 1h-i, 4). Fibre optic illumination enabled the use of low-cost generic microscope objectives (Edmund Optics) designed for inspection applications with working-distances as short as $\sim$ 1mm at 10X magnification (Fig. 1b). These objectives were finite conjugate, requiring only a short light-tight path between the objective and camera. With the optical fibres oriented at a large or near-horizontal angle, the effective axial depth of DUV light penetration into the sample was minimised, improving optical sectioning. The optical fibres were held by a custom-designed 3D-printed optomechanical mount that enabled precise adjustments of illumination direction and angle with up to four degrees of freedom for each fibre, and extremely oblique incident angles of illumination $\sim$85°, achieved with the 10X objective. For the 4X objective, the incident angle of illumination was $\sim$60°. By orientating the fibres obliquely, DUV optical sectioning was improved by $\sim$8.1 times and $\sim$1.4 times, for 10X and 4X setups (compared to a 45° angle of illumination) (Fig. 1d). This illumination design also allowed heatsinking of the LEDs to be far from the sample, which improved LED longevity and reduced potential for thermal damage to samples. Each fibre mount could be optimised for a particular objective and easily hot-swapped. We implemented two optical magnifications − 10X (0.25 NA) for sub-cellular resolution of 0.98 μm, and 4X (0.10 NA) resolution of 2.76 μm for 4X and 10X respectively, for faster imaging over large samples. The illumination could be set to synchronise with the sub-second camera exposure at each image capture in between motorised stage movements, to minimise the high-energy effects of DUV on samples.

2.2 Biomedical applications from cells to tissue

As a unique approach for rapidly imaging unsectioned tissue and thick samples, DUV excitation has much unexplored potential in cell and molecular biology. We found DUV excitation (Fig. 1c) well-suited for a wide range of fluorescent-stained biological sample assays. The few exceptions that did not adequately fluoresce under DUV were calcein AM (live cell stain), certain Alexa Fluor dyes, and certain fluorescent proteins. We demonstrated applications of a fundamental biological assay - the quantitative measurement of cell and tissue viability[20, 21]. As an alternative to the popular calcein and ethidium homodimer assay[22], we used SYTO 9 and propidium iodide (PI) for live/dead cell staining. While this combination is marketed primarily as a bacterial assay, these dyes were also documented to work on eukaryotic cells[23]. Such two-colour assays are a standard quantitative approach for the measurement of cell membrane integrity.

Conventional viability measurements use fluorescent plate readers (spectrophotometers), which give fluorescence intensity readouts summed over entire samples and lack spatial information or cell-level statistics. To demonstrate an automated image-based fluorescence assay for viability, 70% ethanol was added to MCF-7 cells (stained with SYTO 9 and PI) and images at multiple time points over an hour were captured (Fig. 1e). Image analysis yielded a quantitative viability assessment based on automated cell segmentation and pixel-wise colour comparison. Viability imaging on the microscope had single-cell resolution, as opposed to spectrophotometric assays. The same viability assay was also applied successfully to 3D culture and fresh tissue and yielded sharp cellular images from the surface (Fig. 1f-g), with the caveat that information from deeper than the superficial surface could not be obtained. The microscope also facilitates rapid histology-like visualisation of large millimetre-scale to centimetre-scale samples of tissue and organs (Fig. 1h, j, l-m). Histology protocols were designed for but not limited to time-sensitive clinical scenarios, such as surgical resection or biopsy sampling. At 0.5 second camera exposure, a 1 cm^2 sample could be imaged in ∼3 minutes at 4X magnification and ∼8 minutes at 10X magnification. Tissue was stained with fluorescent dyes to help elucidate pattern, shape, and structure, similar to conventional histology staining. Fluorescent colours could be remapped to a clinically relevant stain appearance such as H&E[24, 25] (Fig. 1j, 4a). The microscope is also applicable to protein expression studies in tissue. We demonstrated this capability by immunofluorescence labelling of extracellular matrix proteins in the mouse uterus (Fig. 1k, Supp. Fig. S2).

2.3 Histological studies at organ level

Prior studies had shown close correspondence between DUV-excited fluorescence imaging of tissue samples and histology[13]. For validation of fluorescent images against gold standard H&E, we selected three organ systems for study - renal, digestive, and female reproductive systems (Fig. 2-3). We focused on fresh samples, important in clinical applications and biological viability studies. Images were collected at 10X and 4X, the latter also showing excellent nuclear visualisation at larger fields. Tissue preparation protocols for DUV fluorescence histology did not appear to affect downstream H&E processing (Fig. 2e,h,k, 3e,h,k,n), while images showed a high level of structural correspondence to standard histology. As an aside, we noted that fixed samples could achieve clearer preservation of cellular details and even closer correspondence to histology, but were incompatible with fresh preparations.

The rat cervix is a large structure with complex organisation showing folds, mucosal layering, vasculature, and ductal entrances (Fig. 2a-b), well suited for microscopic mapping. Microscopic quantification such as measurement of the dimensions of vascular structures, staging of follicles, and functional assessment of the uterus could be performed (Fig. 2b,c,f). Oblique illumination provided a shadow effect and a quasi-3D appearance, a unique perspective of the organ revealing the inner surface of the endometrium. The layer of simple columnar epithelial cells lining the endometrium corresponded well to histology. Large field-of-view coverage at cellular resolution enabled quantitative measurements at organ scale that could correlate with physiology or phenotype, such as the size of a follicle indicating maturation (Fig. 2c-e) and endometrial thickness as a marker of estrus cycle staging (Fig. 2f-k). In rat kidneys, renal corpuscles including the Bowman's capsule and glomerular vasculature could be distinguished (Fig. 3a), potentially revealing insights into kidney physiology and injury. Vascular morphology metrics such as calibre and wall thickness could also be assessed (Fig. 2b, 3b), with important relevance to pathology such as vasculitis and stenosis. High-quality *en face* views of the outer (Fig. 3i-k) and inner (Fig. 3l-n) stomach surfaces showed gastric pits and longitudinal muscle respectively. While the visualisation of intact organs is limited to the surface, alternate imaging planes may be developed either by manual cutting or microtome. The cross-sectional structure of the gastric mucosa was studied via a 'Swiss roll' preparation of tissue cut, rolled up and mounted on its side (Fig. 3f-h).

2.4 Fluorescence microtopography

Images, while 2-dimensional, had a quasi-3D effect due to the unsectioned tissue having surface structure and the oblique illumination producing shadows and some depth perception[13]. We exploited this effect to generate a complete 3D reconstruction of the sample surface topography at microscopic resolution (Fig. 1h-i, 4a-b,i-j) using the photometric stereo algorithm. This classic computational technique enabled depth reconstruction from a single fixed field-of-view using fluorescence images excited from multiple different fibre optics directions about the optical axis (Fig. 4e-f). The highly oblique illumination angles provided strong shading that highlighted not only prominent microstructural features such as tubules/ducts but also more minute textural differences that could be associated with tissue/cellular heterogeneity. The illumination from each optical fibre was used to

generate surface topography (Fig. 4g-j), which would otherwise be unobtainable from thin-sectioned tissue or brightfield microscopy and could be rapidly obtained without the need for 3D optical techniques. demonstrated this technique on a cell spheroid, and compared it with an image stack obtained with confocal microscopy (Fig. 4c,d). Features of the derived 3D depth map and confocal stack were qualitatively matched, highlighting the correspondence of DUV fluorescence microtopography by photometric stereo. Quantitative depth measurements and exact surface normal vectors can be obtained (Fig. 4g-h) in principle if illumination angles are precisely known. The illumination intensity may differ slightly between each fibre source, limiting the microtopography render to an imperfect model. While histogram matching can force a more uniform lighting intensity among images, illumination variation sets a limit to the accuracy of depth estimation.

DUV fluorescence microtopography was able to recapitulate the surface contour and finer micro-surface features. As a proof-of-concept, we imaged fixed liver samples, where we reconstructed the 3D structure of blood vessels and surface irregularities from the liver's sinusoidal organisation (Fig. 4a,i). Features such as the blood vessel inner wall and the liver sinusoids' uneven hepatic surface could be observed. The ability to resolve differences in micro-surface topography provided additional information which would otherwise be lost in standard tissue histopathology.

2.5 Investigating antibiotic insult to kidney viability

As a proof-of-concept study of organ-level physiology, we assessed the effects of antibiotic insult on kidney tissue viability. The kidney functions as a major excretory organ for the concentration and elimination of metabolic waste from the body, making it particularly susceptible to cell damage from the cumulative toxic effects of certain drugs[26–28]. We hypothesised that cell viability at the organ-scale could be a surrogate quantitative metric for toxic insults to renal function.

Vancomycin remains a standard treatment of methicillin-resistant *Staphylococcus aureus* (MRSA)[29] despite being linked to nephrotoxicity and acute kidney injury for decades[30–32]. Previous studies had investigated the effects of vancomycin on kidney structure and function, *in vitro* cell-level changes in viability, as well as mechanistic studies[20, 33–36], but there has yet to be a visual representation of kidney tissue viability, apart from area-specific images[33]. Vancomycin is known to affect the proximal convoluted tubules of the kidney nephron due to the drug's mechanism of action [34]. Although the clinical exposure of vancomycin to kidneys occurs during drug clearance in renal excretion and differs from that of our *ex vivo* kidney treatment, the investigation of the effects of antibiotic treatment on specific functional regions could offer us insight into the drug's effect. For this study, we used the standard treatment dosage of 5 mg/mL (Fig. 5d-f) [28, 36–39], a higher dosage of 15 mg/mL, and a PBS control (Fig. 5a-c) on 60 coronal kidney slices (400 μm-thick) obtained from 12 mouse kidneys (Fig. 5g). A common fluorescent live/dead viability assay (SYTO 9 and PI) based on membrane permeability was used to assess kidney slice viability (Fig. 5g). Samples were imaged on our microscope at 4X magnification (Fig. 5a,d,i) which facilitated large-field quantitative mapping.

Image-based viability quantification enabled statistical analysis of treatment groups. Relative pixel-wise comparison of green and red colour channels produced an estimate of the viability of live and dead cells respectively, independent of local and global variation in image brightness (Fig. 5h). To facilitate site-specific analysis, we employed various segmentation strategies for each region-of-interest (Fig. 5h). Both treatment groups had statistically significant ($p < 0.0001$) differences from the control group for all regions (Fig. 5j). The functional regions (corpuscle and tubule) appear to have long-tailed distributions compared to the formal regions (medulla and cortex), showing non-uniform response to treatments. We found a significant ($p < 0.05$) difference between corpuscles and their surrounding tissue (cortex) regardless of treatment group (Fig. 5k), suggesting that the corpuscle viability is uniquely sensitive to environmental factors or sample preparation. Unexpectedly, we did not observe such a difference in the tubules, despite the previously reported incidence of vancomycin-induced nephrotoxicity[34]. This was possibly due to the lack of *in vivo* renal clearance and vancomycin accumulation in the proximal convoluted tubules. We show results from a higher level of drug exposure to demonstrate a potential dosage optimisation study but intentionally avoid comparative claims due to the small sample size for an observed large experimental variation.

This preliminary investigation illustrates the utility of DUV-excited fluorescence image mapping for rapid, quantitative single-cell readouts from large tissue samples and organ sections. This unique approach enables new insights into pharmacological stresses on kidney tissue and its specific functional regions, which are potentially new contributions to an important body of work largely limited to cell culture and clinical studies with little in between. The current resolution of our microscope, whilst limited compared to commercial microscopes,

permits comprehensive analysis and region-specific quantification of large samples. Our compact platform extends standard fluorescence assays previously limited to spectrophotometric measurements into the spatial realm, with the convenience of a benchtop instrument.

3 Discussion

DUV-excited fluorescence microscopy has been rightly celebrated for its simplicity in concept - the combination of oblique DUV illumination and widefield detection. However, prior published illustrations of real-world implementations[15, 16, 19, 40] showed inevitably large and complex setups, with the notable exception of Pocket MUSE, which is generally incompatible with large surgical or meso-scale samples[17]. Our concept of fibre optic-delivered DUV illumination was not only space-conserving but also enabled a number of technical innovations that significantly expand the capabilities of MUSE. Light delivery via a set of small diameter and easily micro-positioned fibre tips greatly relax requirements for long-working-distance objective lenses, and the simplicity of the optical path allows a compact footprint, enabling ease of portability. Multiple sets of optical fibres could be configured for the switching of objectives at different magnifications, allowing us to show results not only at the standard 10X magnification but also fast and high-quality large-field mosaiced image maps at 4X. We anticipate these concepts to broaden options for cost-effective MUSE design and implementation across biomedical scenarios.

Researchers have appreciated the phenomenon of meaningful shadowing produced by oblique DUV illumination, which generated a pseudo-3D effect from coarsely-cut samples and organ surfaces[13]. While omnidirectional illumination would already improve uniformity, we further exploited directional control to produce full 3-dimensional surface reconstruction using photometric stereo[18]. Fluorescence is typically assumed to be Lambertian (isotropic)[41] and has been previously studied as a feasible modality for photometric stereo reconstruction[42]. The ability of MUSE to exclude illumination via imaging optics further prevents non-Lambertian reflectance artefacts. This could have applications in rapidly evaluating the 3D morphology of organoids and 3D culture as they gradually form microstructures of interest, as well as assessing the texture and roughness of organ surfaces or tumours. These microstructures have been reported in other imaging modalities to be a metric of cellular heterogeneity and could have future relevance as a malignancy marker in histopathological evaluation[43, 44]. Tissue microtopography has also been shown to provide favourable paths of low resistance for the translocation of migrating cells from their original site[45]. The translocation of cells includes biologically significant processes such as circulating tumour cells and embryonic development. The ability to distinguish variations in micro-scale topography could be valuable for research and clinical use cases.

While we emphasise the ability to infer histological and biological insights in a large region-of-interest without the need for sectioning, being constrained to surface-level information can be restricting for 3D biological samples; deeper information beyond surface texture is largely unobtainable. We were also only able to image excised tissue samples, limiting our study to only *ex vivo* imaging. Additionally, imaging at higher levels of magnification ($\sim$40x) with our specific range of objectives involves even shorter working-distances and likely requires more sophisticated illumination strategies if not intrinsically limited by the DUV penetration depth.

Although multiple studies have already shown MUSE to generate exquisite images from unsectioned fresh or fixed tissue, our study also featured a number of examples. This is partly to demonstrate our unique optical design with no-brand lensing to be competitive with the state of the art and also to present a few new perspectives based on large-field mapping - namely, the thorough histological study of selected organ systems, and quantitative studies of fluorescence images, both of which are particularly crucial for applications in translational biology. While we acknowledge that fixation is ideal for visualisation, we focused on fresh and live biological preparations to study their viability and also to define a translational step towards envisioning DUV excitation for live samples and *in vivo* models. Real-time sample imaging could have potential clinical applications in surgery including anastomotic viability and margin evaluation. While mutagenic effects of DUV light are well-known, the very brief sub-second exposures needed for high-quality imaging may be tolerable, and motivate dosing studies. Given concurrent advances in DUV light sources, fibre optics and microscopy, the potential of minimally invasive ultraviolet endoscopy[46] for real-time cellular interrogation of living organs could be due for a revisit.

4 Methods

4.1 Microscope design and components

The deep ultraviolet (DUV) fibre optic fluorescence microscope platform was based on an epi-illuminated inverted microscope design. The microscope sat on a 30x30 cm optical breadboard and comprised the illumination, optical, sample holder, and mechanical and electrical components.

Illumination components DUV illumination at a peak wavelength of 277 nm was produced by DUV LEDs (ILR-OV01-O275-LS030-SC201.; Osram) powered by a constant 700 mA current supply (RECOM) and cooled with a heat sink (Intelligent LED Solutions). Magnetic butt-coupling of multi-mode optical fibres (57-070; Edmund Optics), with an outer diameter of ~ 710 μm, to the light-emitting diodes (LEDs) was achieved with a custom 3D-printed magnetic fibre coupler (Supp. Fig. S1). The magnetic coupler allowed hot swapping of the illumination source and the optical fibres. The four magnetically butt-coupled optical fibres had a combined measured output power of around 6.29 mW and a coupling efficiency of roughly 4.6%. Up to two fibre optics were coupled to a single LED, although the combined coupling efficiency remained at roughly 5%. The opposing DUV-emitting end of the fibre optic was controlled via a 3D-printed custom optomechanical fibre holder jig which provided four degrees of freedom, allowing fine control and angle adjustments of the fibre to be made for uniform sample illumination. The extreme oblique incident angle of illumination ($\sim 85°$) was used in the 10X objective setup. The incident angle of illumination was ($\sim 60°$) for the 4X objective setup. The area of illumination for the 10X and the 4X setup was measured to be approximately 4.88 mm^2 and 8.58 mm^2 respectively. The intensity of the 10X and the 4X setup was calculated to be approximately 1.29 mW/mm^2 and 0.733 mW/mm^2 respectively. Figures 1b-d were created with BioRender.com.

Optical components Digital images were taken using a colour camera (BFS-U3-120S4C-CS; Teledyne FLIR) magnified by either 10X or 4X finite conjugate DIN objectives (43-907, 67-706; Edmund Optics). The numerical aperture and working-distances for the 10X and 4X objectives were 0.25, 1.5 mm and 0.10, 15.25 mm respectively. A custom 3D-printed objective holder was non-mechanically coupled to a tube assembly (54-868; Edmund Optics), enabling hot swapping between the 10X and 4X objective setups. The objective holder included a filter slot which enabled the suppression of specific wavelengths which could minimise unwanted signals including autofluorescence from samples. The tube assembly connected the objective holder with the colour camera. The effective resolution was measured on a USAF 1951 resolution target to have a 13.6% contrast level at Group 9 Element 1, corresponding to a resolution of 0.977 μm (10X), and 12.0% contrast level at Group 7 Element 4, corresponding to a resolution of 2.76 μm (4X). The clear resolution target was imaged by placing a piece of plain white paper behind the resolution target. The autofluorescence of the plain paper, in the presence of the DUV excitation, provided the backlight illumination of the resolution target. The effective field-of-view was determined to be 0.748 by 0.561 mm (10X) and 1.85 by 1.39 mm (4X) by imaging a checkerboard calibration target.

Sample holder components Histology cassettes and 6-well plates were both modified to include a 150 μm thick UV-transmissible quartz window to contain tissue and cell samples respectively. A custom-machined steel sample holder supported by four optical posts was used to mount the histology cassettes and 6-well plates. The standard histology cassettes were modified by cutting a hole approximately 11x20 mm before applying liquid epoxy to adhere a quartz coverslip (JGS2, Latech) to the outer surface covering the hole. The quartz coverslips acted as a flat and UV-transmissible surface for samples to be placed on for imaging. The 6-well plates (3516, Corning) were similarly modified by drilling a 7 mm circular window through the bottom of each well and having the quartz coverslip glued using liquid epoxy to cover the window. Cells were seeded directly on the modified 6-well plates and imaged directly on the quartz coverslip window.

Mechanical and Electrical Components X-axis and Y-axis movement, at sub-micrometer precision, of the sample relative to the camera was enabled by mounting the sample holder on a stack of two manual linear translation stages. Z-axis movement was enabled by attaching the optical components of the system to a manual vertical translation stage. Two 3D-printed stepper motor holders and stepper motor couplers were designed to co-axially couple the stepper motors to the micrometre knob of the stage. A microcontroller controlled the stepper motor by either parsing a set of sequential instructions allowing for automated stage movement or inputs from an analogue stick for manual stage movement of the microscope in the X and Y direction. The flashing of the LEDs was controlled by the microcontroller during image acquisition, synchronised to the camera's exposure time, to reduce unwanted DUV exposure to samples during stage movement of the automated imaging process.

4.2 Biological applications

Biological sample preparation Human breast adenocarcinoma epithelial MCF-7 cell line was purchased from the American Type Culture Collection (ATCC). Cells were cultured in RPMI Medium 1640 (22400089, Gibco) supplemented with 10% fetal bovine serum (FBS-HI-12A, Capricorn Scientific), 100 U/mL penicillin and 100 $\mu g/mL$ streptomycin (15140-122, Gibco) in 5% CO2 at $37°C$. Formation of spheroids was induced by seeding MCF-7 cells at 2x10^4 cells/well, in 96-well U-bottomed ultra-low attachment plates (174929, Life Technologies) with shaking for 2-3 days. For tissue samples, female NCr nude mice were euthanised at the humane or experimental endpoint of a separate study in accordance with the approved A*STAR Institutional Animal Care and Use Committee (IACUC) protocol. Mice were dissected and routine post-study tissue collection was performed. Alternatively, whole mice and rats carcasses or specific harvested organs were purchased (InVivos). Organs were harvested and washed in 1X Phosphate Buffered Saline (PBS) (BUF-2040-10X4L, 1st BASE), and sliced either using a vibratome (VF500-0Z, Precisionary Instruments) or manually using a scalpel depending on the use case. For vibratome slicing, the organ was embedded in 2% Type I-B agarose (Sigma Aldrich). In brief, the sample was glued onto the plunger of the specimen tube, liquid agarose was pipetted in excess to cover the tissue before the agarose was solidified using a chilling block. The specimen tube containing the sample was loaded onto the vibratome and sliced into 400 μm to 1 mm-thick slices at various oscillation and sectioning speeds depending on the organ type. Surrounding agarose was delicately removed using forceps before staining, with Hoechst and Rhodamine B for histological studies or SYTO 9 and propidium iodide (PI) for viability studies (Supp. Fig. S2).

Histological studies Hoechst 33342 (62249, Thermofisher Scientific) and Rhodamine B (A5102, TCI) fluorescence stains were prepared at various concentrations for optimal staining of different tissue types. Tissue samples were stained for 1 minute, before being washed in 1X PBS twice, for 30 seconds each. Samples were blotted dry with Kimwipes and placed on modified histology cassettes for imaging. 0.1 mg/mL Hoechst with 2 mg/mL Rhodamine B was identified as an effective fluorescent concoction for general staining over a wide range of fresh and fixed murine tissue including organs like the heart, liver, stomach, and kidney, as well as the female reproductive tract. 0.1 mg/mL Hoechst with 4 mg/mL Rhodamine B was also used to more strongly contrast the structural features of organs such as the tubules of fresh kidneys. Organs which featured a high level of nuclear concentration such as the ovaries and gastric surface of the stomach were better highlighted with a lower level of nuclear stain ratio of 0.1 mg/mL Hoechst with 1 mg/mL Rhodamine B and 0.05 mg/mL Hoechst with 2 mg/mL Rhodamine B respectively.

Single Cell Viability Demonstration We seeded 1x10^6 cells/mL MCF-7 cells onto modified 6-well plates. Prior to imaging, media was removed and cells were stained with a total of 750 μL of viability stains 1:1 SYTO 9 and PI nucleic acid stain (1.5 μL SYTO 9 to 1.5 μL PI per 1 mL PBS) for 15 minutes (L7007, LIVE/DEAD™ BacLight™ Bacterial Viability Kit, for microscopy, Invitrogen). At the point of imaging, 250 μL of 70% ethanol was added to induce cell death. Images of cells were acquired every minute over 60 minutes.

Kidney Viability Study We harvested 12 kidneys harvested from 6 mice and classified them into 3 treatment groups, control, low dose of vancomycin (5 mg/mL), and high dose of vancomycin (15 mg/mL). The fresh kidneys were sliced coronally into 400 μm-slices to obtain 5 mid-section slices per kidney, totalling 60 slices. Samples in the treatment group were treated with vancomycin (vancomycin hydrochloride, 1709007, US Pharmacopeia) for 1 hour. After treatment, sections were washed in PBS before incubating in 5:1 SYTO 9 and PI nucleic acid stain (7.5 μL for 15 minutes with shaking. Samples were blotted dry with Kimwipes and placed on modified histology cassettes for imaging. Methods are illustrated in Figure 5g, created with BioRender.com. Kidney model in Figure 5i was obtained from Sketchfab[47].

Viability quantification Our general strategy for image-based viability quantification involves 2 stages: segmentation followed by pixel-wise relative green and red comparison (Fig. 5h). Specific segmentation strategies differ for each use case. Colour comparisons begin with first splitting the colour image into its red, blue, and green (RGB) channels. A map of pixels where the green channel has a higher intensity than the red channel represents the live regions of the tissue (Fig. 5h) is then created. This is a convenient strategy as the viability assay of choice stains in green (SYTO 9) and red (PI) at similar intensities. Since PI is only permeable to dead cells and has a stronger affinity for nucleic acids[48], the point where the red signal is greater than the green represents a significant uptake of PI and thus differentiates dead cells from live ones. This strategy is also robust to any local and global variation in brightness that tends to happen during the imaging process.

Single cells were segmented using Otsu's method of thresholding before pixel-wise relative colour comparison. Kidneys were segmented from their background using constant thresholding. Kidney regions of interest like

the cortex, medulla, corpuscles, and proximal convoluted tubules were cropped using various strategies. The cortex and medullas were manually cropped using ImageJ for 12 kidney slices per group with visible cortical and medullary regions. All discernible longitudinal proximal convoluted tubules were manually cropped from each kidney sample due to their non-uniform shape. Corpuscles were detected using template matching and cropped to a fixed size, generating over 4,777 crops. The Welch Two Sample t-test was used to determine the statistically significant differences between treatment groups (Fig. 5j,k). Statistical tests and plots were done using R programming language and Tidyverse [49].

Immunohistochemistry Mouse uterus cross-section tissue (1 mm) was fixed for 30 minutes in 4% formaldehyde (VWR) before blocking and permeabilisation for 2 hours in 1% BSA (W384A, Promega) and 0.5% Triton-X (H5141, Promega) for 2 hours. Thereafter, primary antibodies 1/100 Anti-Fibronectin (ab2413, Abcam) and Anti-Laminin (ab2466, Abcam) were added to the uterus slices and incubated for 16 hours. The slices were washed twice in 1X PBS, 5 minutes each, before secondary antibodies 1/100 Alexa-Fluor 594 (ab150160, Abcam) and Alexa-Fluor 488 (A11034, Life Technologies) were applied and left to incubate for 5 hours. After incubation, samples were washed twice in 1X PBS for 5 minutes prior to imaging.

4.3 Image acquisition and large-field mosaicing

Imaging settings and processing Colour images were captured with exposure ranging between 0.1 to 3 seconds. The images were saved in PNG file format. Image processing was done with the open-source ImageJ (Fiji)[50] and limited to brightness and contrast, colour balance, and despeckling to remove hot pixels artefacts from the colour camera. No background correction, subtraction or deconvolution was performed on the images.

Automated image acquisition Image acquisition was facilitated by the integration of C code on the Arduino, Python code on a laptop attached to the microscope, and the Teledyne FLIR Spinnaker SDK. Manual image acquisition was done using an analogue stick with the Arduino for motor control and the SpinView application from the Spinnaker SDK for the viewing and saving of images. Automated image acquisition for large mosaic images was coordinated by our custom Python software. It received and processed user input, then controlled the camera through the Python interface from the Spinnaker SDK and the stage by sending condensed instructions to the Arduino.

Large-field mosaicing Large-field mosaicing was enabled by the Python software integrated with the microscope and the freely available Microsoft Image Composite Editor. Images were automatically and sequentially captured with an adjustable overlap (usually set at 10%/15% margins) and stitched together using Image Composite Editor to achieve gigapixel-sized mosaic images comprising hundreds of individual images. The sample stage was precise enough for images to be manually focused prior to imaging, with the Python software subsequently automatically controlling the stepper motors movement, flashing of the DUV LEDs, and the camera capture of images, without additional refocusing required, over the entire sample area.

4.4 3D microtopography with photometric stereo

Sequential illumination and image acquisition To obtain the micro-topographical information over a region-of-interest on a sample, each of the four fibre optics was coupled to an independently controlled DUV LED. A reference image of the region-of-interest was then captured with illumination coming from all the fibre optics. Four sequential images with directional illumination from each fibre optics were obtained while maintaining the same field-of-view over the region-of-interest. The exposure of these four sequential images was increased (up to 3 seconds exposure) compared with the reference image, to compensate for the dimmer illumination coming from a single fibre optic.

Image processing Despeckling was performed on all images using ImageJ to remove hot pixels artefact as the bright pixels which would affect the subsequently obtained surface normals map. Following this, the four sequential images were histogram-matched with the reference image to obtain the different direction-of-illumination images with the same relative brightness. Histogram matching was done to force a more uniform brightness between the four images given there were slight variations in illumination intensity between each of the four optical fibres.

Photometric stereo for surface normals and depth map With the four histogram-matched different

direction-of-illumination images, four representative vectors for each direction of fibre optic illumination were then inputted into our implementation of the photometric stereo algorithm (vectorised and ported to Python based on an open-source Matlab implementation [51]). The four representative vectors reflected the 90 °rotation about the image's centre to match our setup's fibre orientation (Fig. 4e, created with BioRender.com.). The photometric stereo algorithm produced the surface normals and depth map of the region-of-interest. It was noted that changing the input vector angle of illumination (obliqueness of illumination angle) did not significantly affect the obtained depth map as the depth map displayed the normalised depth rather than true depth. The depth map was rendered in 3D, with either the H&E recoloured image or the despeckled reference image used as the surface texture in PyVista, to produce an interactive 3D micro-topographical reconstruction of the sample region-of-interest.

5 Acknowledgements

This work was supported by the Singapore National Research Foundation Fellowship (NRFF13-2021-0057) and the Agency for Science, Technology and Research (A*STAR). We would like to thank Dr Ong Chee Bing for his invaluable support and pathology-related consultations, Stefanie Zi En Lim, Jeremy Rui Quan Lee, and Dr Nazihah Husna Abdul Aziz for their contributions to data preparation, Li Qin Shen for her contributions to software development for microscope automation, Rachel Yixuan Tan for her contributions to initial mechanical designs, and Dr Zesheng Zheng for engineering-related consultations.

6 Bibliography

References

1. Bhatia, H. S. *et al.* Spatial proteomics in three-dimensional intact specimens. *Cell* **185.** Publisher: Elsevier, 5040–5058.e19 (Dec. 22, 2022).
2. Rao, A., Barkley, D., França, G. S. & Yanai, I. Exploring tissue architecture using spatial transcriptomics. *Nature* **596.** Number: 7871 Publisher: Nature Publishing Group, 211–220 (Aug. 2021).
3. Ragazzi, M. *et al.* Fluorescence confocal microscopy for pathologists. *Modern Pathology* **27.** Number: 3 Publisher: Nature Publishing Group, 460–471 (Mar. 2014).
4. Tao, Y. K. *et al.* Assessment of breast pathologies using nonlinear microscopy. *Proceedings of the National Academy of Sciences of the United States of America* **111,** 15304–15309 (Oct. 28, 2014).
5. Glaser, A. K. *et al.* A hybrid open-top light-sheet microscope for versatile multi-scale imaging of cleared tissues. *Nature Methods* **19.** Number: 5 Publisher: Nature Publishing Group, 613–619 (May 2022).
6. Voskuil, F. J. *et al.* Intraoperative imaging in pathology-assisted surgery. *Nature Biomedical Engineering* **6.** Number: 5 Publisher: Nature Publishing Group, 503–514 (May 2022).
7. Lemon, W. C. & McDole, K. Live-cell imaging in the era of too many microscopes. *Current Opinion in Cell Biology. Cell Dynamics* **66,** 34–42 (Oct. 1, 2020).
8. Li, Y. *et al.* Hematoxylin and eosin staining of intact tissues via delipidation and ultrasound. *Scientific Reports* **8,** 12259 (Aug. 16, 2018).
9. Wang, J., Xu, Y. & Boppart, S. A. Review of optical coherence tomography in oncology. *Journal of Biomedical Optics* **22,** 1–23 (Dec. 2017).
10. Ming, Y. *et al.* Longitudinal morphological and functional characterization of human heart organoids using optical coherence tomography. *Biosensors & Bioelectronics* **207,** 114136 (July 1, 2022).
11. Costa, P. C. *et al.* Towards in-vivo label-free detection of brain tumor margins with epi-illumination tomographic quantitative phase imaging. *Biomedical Optics Express* **12.** Publisher: Optica Publishing Group, 1621–1634 (Mar. 1, 2021).
12. Lin, B., Urayama, S., Saroufeem, R. M. G., Matthews, D. L. & Demos, S. G. Real-time microscopic imaging of esophageal epithelial disease with autofluorescence under ultraviolet excitation. *Optics Express* **17.** Publisher: Optica Publishing Group, 12502–12509 (July 20, 2009).
13. Fereidouni, F. *et al.* Microscopy with ultraviolet surface excitation for rapid slide-free histology. *Nature Biomedical Engineering* **1.** Number: 12 Publisher: Nature Publishing Group, 957–966 (Dec. 2017).

14. Yoshitake, T. *et al.* Rapid histopathological imaging of skin and breast cancer surgical specimens using immersion microscopy with ultraviolet surface excitation. *Scientific Reports* **8.** Number: 1 Publisher: Nature Publishing Group, 4476 (Mar. 14, 2018).

15. Xie, W. *et al.* Microscopy with ultraviolet surface excitation for wide-area pathology of breast surgical margins. *Journal of Biomedical Optics* **24,** 026501 (Feb. 2019).

16. Guo, J., Artur, C., Womack, T., Eriksen, J. L. & Mayerich, D. Multiplex protein-specific microscopy with ultraviolet surface excitation. *Biomedical Optics Express* **11.** Publisher: Optica Publishing Group, 99–108 (Jan. 1, 2020).

17. Liu, Y., Rollins, A. M., Levenson, R. M., Fereidouni, F. & Jenkins, M. W. Pocket MUSE: an affordable, versatile and high-performance fluorescence microscope using a smartphone. *Communications Biology* **4.** Number: 1 Publisher: Nature Publishing Group, 1–14 (Mar. 12, 2021).

18. Woodham, R. Photometric method for determining surface orientation from multiple images. *Optical Engineering* **19,** 139–144 (Jan. 1, 1980).

19. Qorbani, A. *et al.* Microscopy with ultraviolet surface excitation (MUSE): A novel approach to real-time inexpensive slide-free dermatopathology. *Journal of Cutaneous Pathology* **45.** _eprint: https://onlinelibrary.wiley.com/doi/ 498–503 (2018).

20. Arimura, Y. *et al.* Mitochondrial superoxide production contributes to vancomycin-induced renal tubular cell apoptosis. *Free Radical Biology and Medicine* **52,** 1865–1873 (May 2012).

21. Braun, J. *et al.* Toxic Effect of Vancomycin on Viability and Functionality of Different Cells Involved in Tissue Regeneration. *Antibiotics* **9,** 238 (May 8, 2020).

22. Bariteau, J. T., Kadakia, R. J., Traub, B. C., Viggeswarapu, M. & Willett, N. J. Impact of Vancomycin Treatment on Human Mesenchymal Stromal Cells During Osteogenic Differentiation (2018).

23. *LIVE/DEAD BacLight Bacterial Viability Kits* `https://www.thermofisher.com/order/catalog/product/l7007`.

24. Giacomelli, M. G. *et al.* Virtual Hematoxylin and Eosin Transillumination Microscopy Using Epi-Fluorescence Imaging. *PLOS ONE* **11.** Publisher: Public Library of Science, e0159337 (Aug. 8, 2016).

25. Serafin, R., Xie, W., Glaser, A. K. & Liu, J. T. C. FalseColor-Python: A rapid intensity-leveling and digital-staining package for fluorescence-based slide-free digital pathology. *PLOS ONE* **15.** Publisher: Public Library of Science, e0233198 (Oct. 1, 2020).

26. Rodvold, K. A. *et al.* Vancomycin pharmacokinetics in patients with various degrees of renal function. *Antimicrobial Agents and Chemotherapy* **32,** 848–852 (June 1988).

27. Dieterich, C. *et al.* Gene expression analysis reveals new possible mechanisms of vancomycin-induced nephrotoxicity and identifies gene markers candidates. *Toxicological Sciences: An Official Journal of the Society of Toxicology* **107,** 258–269 (Jan. 2009).

28. Pais, G. M. *et al.* Vancomycin-Induced Kidney Injury: Animal Models of Toxicodynamics, Mechanisms of Injury, Human Translation, and Potential Strategies for Prevention. *Pharmacotherapy: The Journal of Human Pharmacology and Drug Therapy* **40,** 438–454 (May 2020).

29. Rose, W., Volk, C., Dilworth, T. J. & Sakoulas, G. Approaching 65 Years: Is It Time to Consider Retirement of Vancomycin for Treating Methicillin-Resistant Staphylococcus aureus Endovascular Infections? *Open Forum Infectious Diseases* **9,** ofac137 (May 2022).

30. Bamgbola, O. Review of vancomycin-induced renal toxicity: an update. *Therapeutic Advances in Endocrinology and Metabolism* **7,** 136–147 (June 2016).

31. Luque, Y. *et al.* Vancomycin-Associated Cast Nephropathy. *Journal of the American Society of Nephrology* **28,** 1723–1728 (June 2017).

32. Giehl, N., Nobakht, N., Kamgar, M. & Zuckerman, J. Minimizing Vancomycin-Associated Acute Interstitial Nephritis (2022).

33. Crawford, C. *et al.* An Intact Kidney Slice Model to Investigate Vasa Recta Properties and Function in situ. *Nephron Physiology* **120,** p17–p31 (July 20, 2012).

34. Humanes, B. *et al.* Protective Effects of Cilastatin against Vancomycin-Induced Nephrotoxicity. *BioMed Research International* **2015,** 704382 (2015).

35. Pais, G. M. *et al.* Lack of synergistic nephrotoxicity between vancomycin and piperacillin/tazobactam in a rat model and a confirmatory cellular model. *Journal of Antimicrobial Chemotherapy* **75,** 1228–1236 (May 1, 2020).

36. Yu, P. *et al.* N-acetylcysteine Ameliorates Vancomycin-induced Nephrotoxicity by Inhibiting Oxidative Stress and Apoptosis in the in vivo and in vitro Models. *International Journal of Medical Sciences* **19,** 740–752 (2022).

37. Khalili, H., Bairami, S. & Kargar, M. Antibiotics induced acute kidney injury: incidence, risk factors, onset time and outcome. *Acta Medica Iranica* **51,** 871–878 (2013).

38. Zamoner, W., Prado, I. R. S., Balbi, A. L. & Ponce, D. Vancomycin dosing, monitoring and toxicity: Critical review of the clinical practice. *Clinical and Experimental Pharmacology and Physiology* **46,** 292–301 (Apr. 2019).

39. He, J. *et al.* Vitamin C reduces vancomycin-related nephrotoxicity through the inhibition of oxidative stress, apoptosis, and inflammation in mice. *Annals of Translational Medicine* **9,** 1319–1319 (Aug. 2021).

40. Ching-Roa, V. D., Huang, C. Z. & Giacomelli, M. G. Improved microscopy with ultraviolet surface excitation (MUSE) using high-index immersion illumination. *Biomedical Optics Express* **12,** 6461–6473 (Sept. 22, 2021).

41. Treibitz, T., Murez, Z., Mitchell, B. G. & Kriegman, D. *Shape from Fluorescence* in *Computer Vision – ECCV 2012* European Conference on Computer Vision (Springer, Berlin, Heidelberg, 2012), 292–306.

42. Salvant, J. *et al. Photometric Stereo by UV-Induced Fluorescence to Detect Protrusions on Georgia O'Keeffe's Paintings* Nov. 21, 2017.

43. Davnall, F. *et al.* Assessment of tumor heterogeneity: an emerging imaging tool for clinical practice? *Insights into Imaging* **3,** 573–589 (Oct. 24, 2012).

44. Bashir, U., Siddique, M. M., Mclean, E., Goh, V. & Cook, G. J. Imaging Heterogeneity in Lung Cancer: Techniques, Applications, and Challenges. *AJR. American journal of roentgenology* **207,** 534–543 (Sept. 2016).

45. Dai, W. *et al.* Tissue topography steers migrating Drosophila border cells. *Science* **370.** Publisher: American Association for the Advancement of Science, 987–990 (Nov. 20, 2020).

46. Smith, B. H. & Edward Berk, J. The detection of upper gastrointestinal bleeding sites by ultraviolet endoscopy. *Gastrointestinal Endoscopy* **19,** 123–124 (Feb. 1, 1973).

47. *kidney (ren) pig - Download Free 3D model by vetanatMunich* May 11, 2020.

48. Stiefel, P., Schmidt-Emrich, S., Maniura-Weber, K. & Ren, Q. Critical aspects of using bacterial cell viability assays with the fluorophores SYTO9 and propidium iodide. *BMC Microbiology* **15,** 36 (Dec. 2015).

49. Wickham, H. *et al.* Welcome to the tidyverse. *Journal of Open Source Software* **4,** 1686 (2019).

50. Schindelin, J. *et al.* Fiji: an open-source platform for biological-image analysis. *Nature Methods* **9.** Number: 7 Publisher: Nature Publishing Group, 676–682 (July 2012).

51. Zhang, X. A MATLAB Implementation of the Basic Photometric Stereo Algorithm. *https://github.com/xiumingzhang/ph stereo.* original-date: 2015-04-19T14:36:39Z (Dec. 19, 2022).

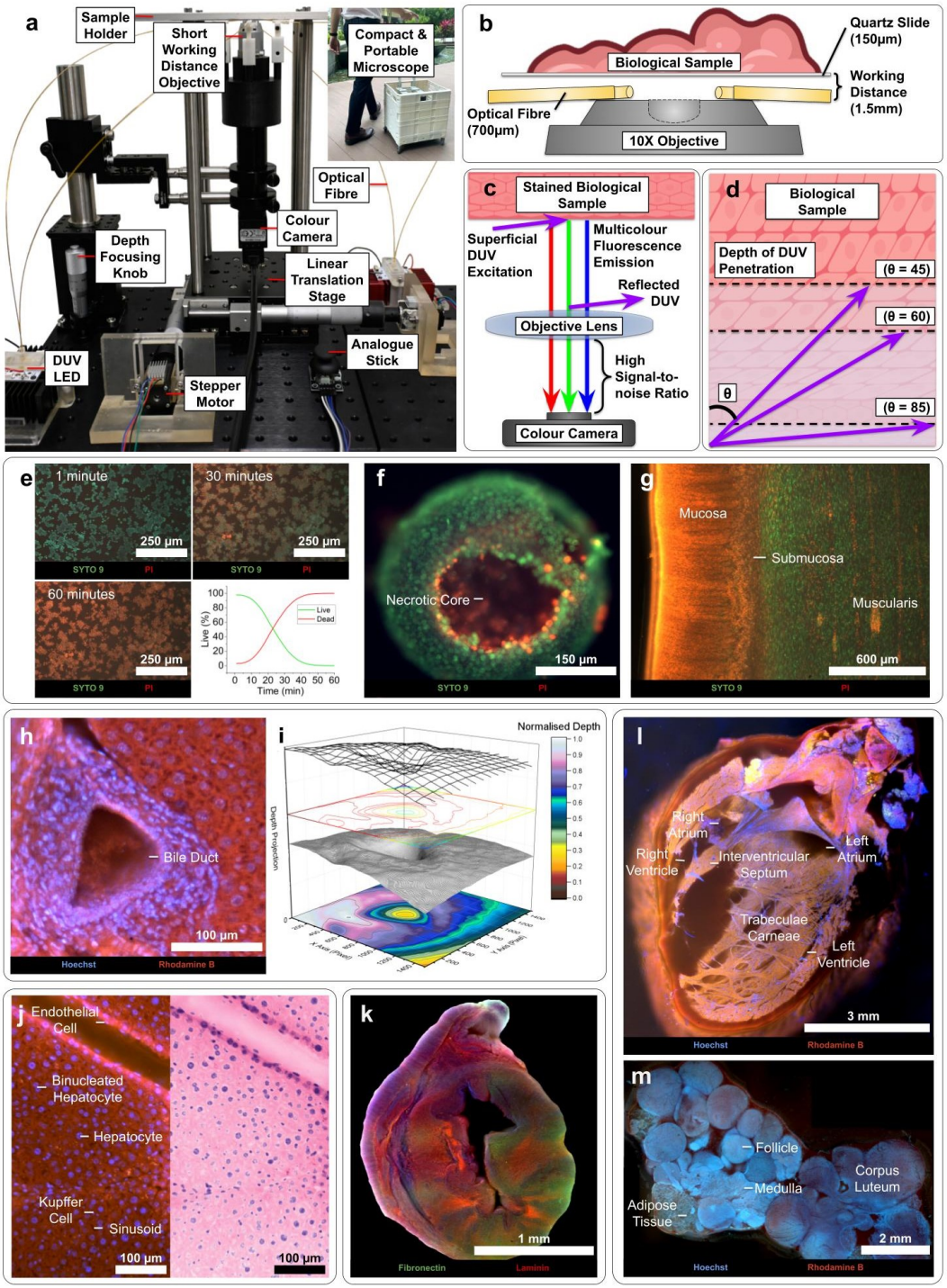

Figure 1: Overview of microscope and capabilities. a. Key components of the microscope. Optical fibres carry Deep Ultraviolet (DUV) light from LEDs to the sample. b. Fibres allow for oblique epi-illumination via short working distances. c. DUV superficially excites the surface of stained biological tissue, producing multi-colour fluorescence emissions. Glass objective lens excludes DUV, producing images with a high signal-to-noise ratio. d. Oblique angles of illumination improve the optical sectioning capabilities of DUV. e. Quantification of single cell (MCF-7) % viability over time after exposure to chemical insult [green SYTO 9 stain, live; red propidium iodide (PI) stain, dead]. f. Spheroid (MCF-7) imaging showed a red necrotic core contrasting with the green proliferative layer. g. Viability staining can highlight tissue structure despite primarily staining cell nuclei. The mucosa, submucosa and muscularis mucosa of a fresh mouse stomach can be identified. h-i. Fluorescence image and 3D reconstruction of formalin-fixed mouse liver (blue stain, nucleus stain Hoechst 33342; red-orange stain, counterstain rhodamine B). A strong quasi-3D effect is observed, with the highly nucleated bile duct extending deeper into the tissue. The 3D depth map was obtained using photometric stereo. j. Fluorescence image (left) of formalin-fixed mouse liver (blue stain, nucleus stain Hoechst 33342; red-orange stain, counterstain rhodamine B) with the corresponding virtual H&E recoloured image (right). Hepatocytes and sinusoids are distinguishable. Flat nuclei of endothelial cells are seen lining the vein. k. Multiplexed image of fixed mouse uterus with immunohistochemical staining for fibronectin (green) and laminin (red) of the extracellular matrix. The blue signal originates from the autofluorescence of the fixed tissue. l. Large field-of-view mosaics enable whole organ visualisation of a fresh mouse heart at 4X magnification and millimetre-scale (blue stain, nucleus stain Hoechst 33342; red-orange stain, counterstain rhodamine B). The coronal section displays the four main chambers and architectural organisation of the trabeculae carneae on the endocardial surface with a quasi-3D perspective. m. Freshly excised rat ovary reveals follicles at different developmental stages and associated features of the ovary.

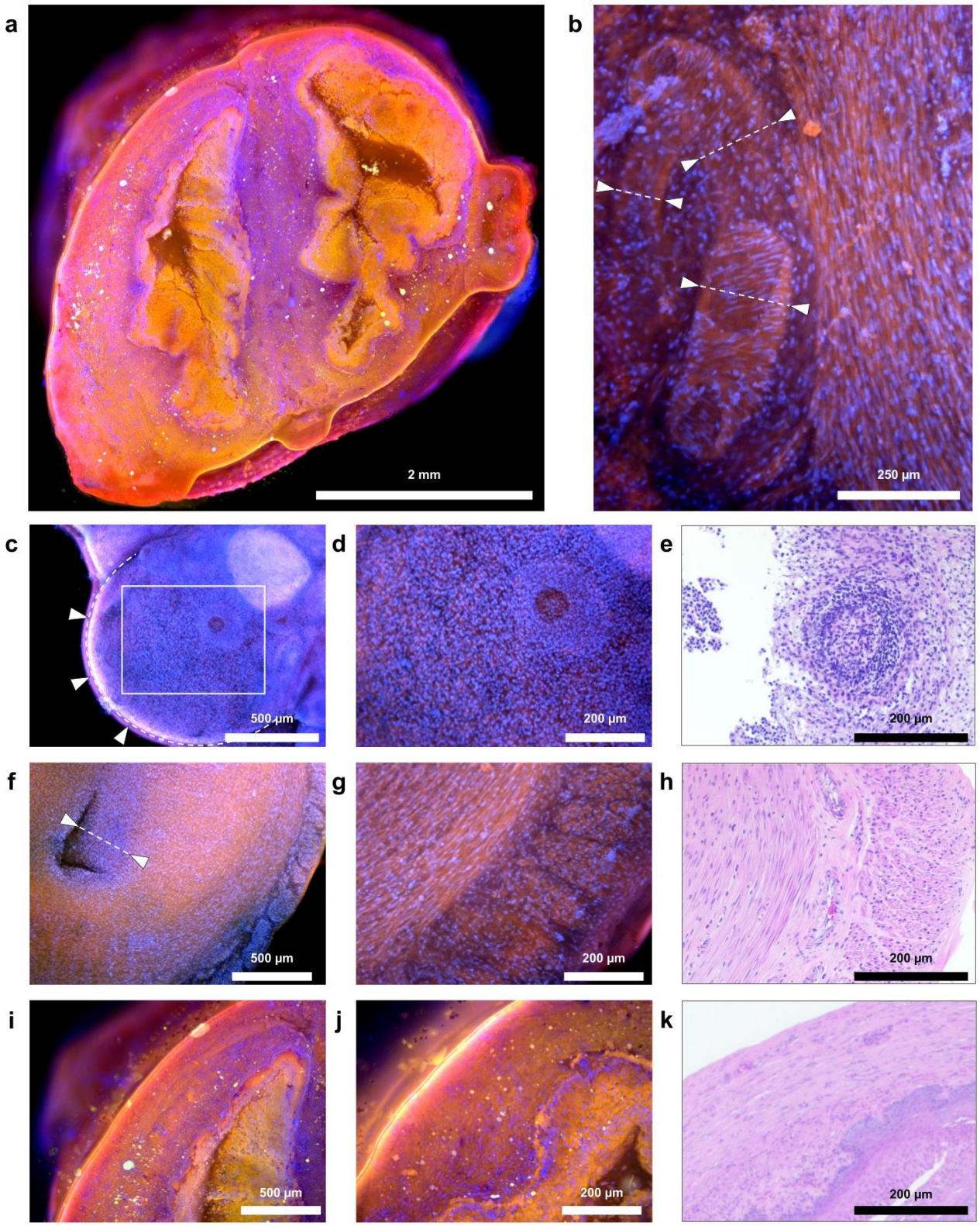

Figure 2: The female reproductive tract. a. Cut surface of a fresh rat cervix that reveals the merging of two uterine horns distal to the uterine junction. The inner surface of the endometrium is visibly textured (blue stain, nucleus stain Hoechst 33342; red-orange stain, counterstain rhodamine B). b. Three interlacing blood vessels located in the stratum vasculare of fresh rat uterus at 10X magnification. The vessels have an approximate diameter of 140 μm, 130 μm, and 75 μm with a wall thickness of 25 μm, 25 μm and 18 μm respectively. c-e. 4X and 10X images and corresponding H&E histology of the intact surface from the same fresh rat ovary, with a developing secondary follicle, is identified by the multi-cell thickness at the edge of the follicle and a measured diameter of 1160 μm. At a higher magnification, the granulosa layer is distinct with clear visualisation of the oocyte eccentrically positioned. f-h. 4X and 10X images and corresponding H&E histology of the cut surface of the same fresh rat uterus, with all three layers (perimetrium, myometrium, endometrium) of the uterus clearly visible and distinguishable from each other. The uterus has a measured radius of approximately 1410 μm with the stratum functionalis being roughly 350 µm thick, measurements that could be used in aiding the staging of the estrus cycle. At higher magnification, the inner circular layer of smooth muscles transitions to the outer longitudinal layer of smooth muscles in the myometrium, separated by stratum vasculare. i-k. 4X, and 10X images and corresponding H&E histology of the same fresh rat cervix showing the lumen of a single uterine horn.

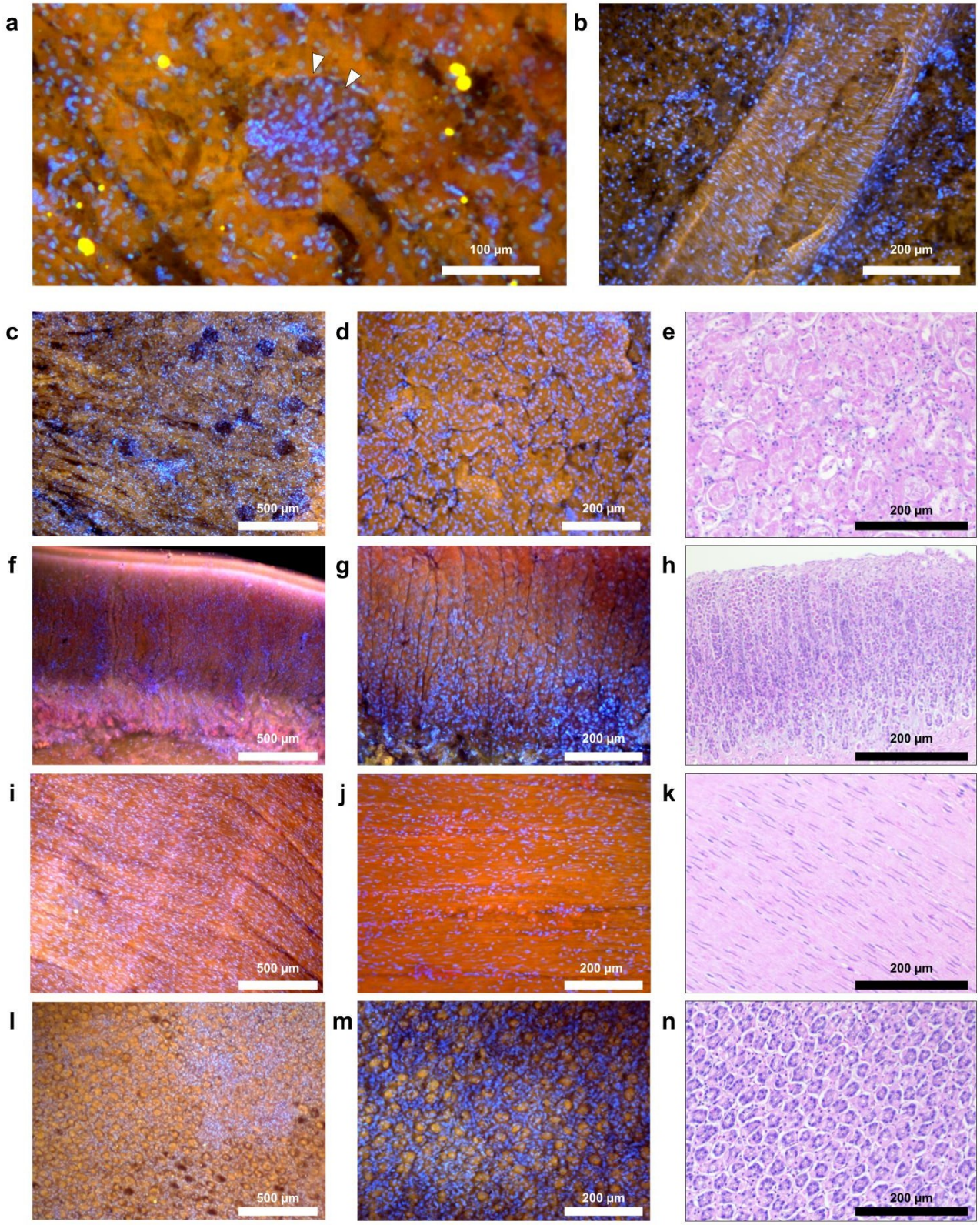

Figure 3: The kidney and stomach. a. Renal glomerulus in a fresh mouse kidney, note the epithelial parietal cells (white arrowheads) of Bowman's capsule (blue stain, nucleus stain Hoechst 33342; red-orange stain, counterstain rhodamine B). b. Partially cut surface of a large blood vessel from a fresh mouse kidney, revealing the inner surface of a blood vessel. c. Kidney cortex of a fresh mouse kidney, showing multiple renal corpuscles at 4X magnification. d. *Enface* surface of fresh mouse renal tubules at 10X magnification. e. Corresponding H&E of the same sample, showing the renal tubules. f-h. 4X and 10X images and corresponding H&E histology of the same fresh rat stomach. The distinct organisation of cells of the stomach mucosa can be observed extending from the lumen to the deeper submucosa layer. i-k. 4X and 10X images and corresponding H&E histology of the muscularis externa of the same fresh rat's stomach. The nuclei of the smooth muscle cells from the outer longitudinal layer can be clearly visualised at both 4X and 10X. l-n. 4X and 10X images and corresponding H&E histology of gastric pits on the inner surface of the same fresh rat stomach. Higher magnification of the lumen reveals surface mucous cells forming the gastric openings.

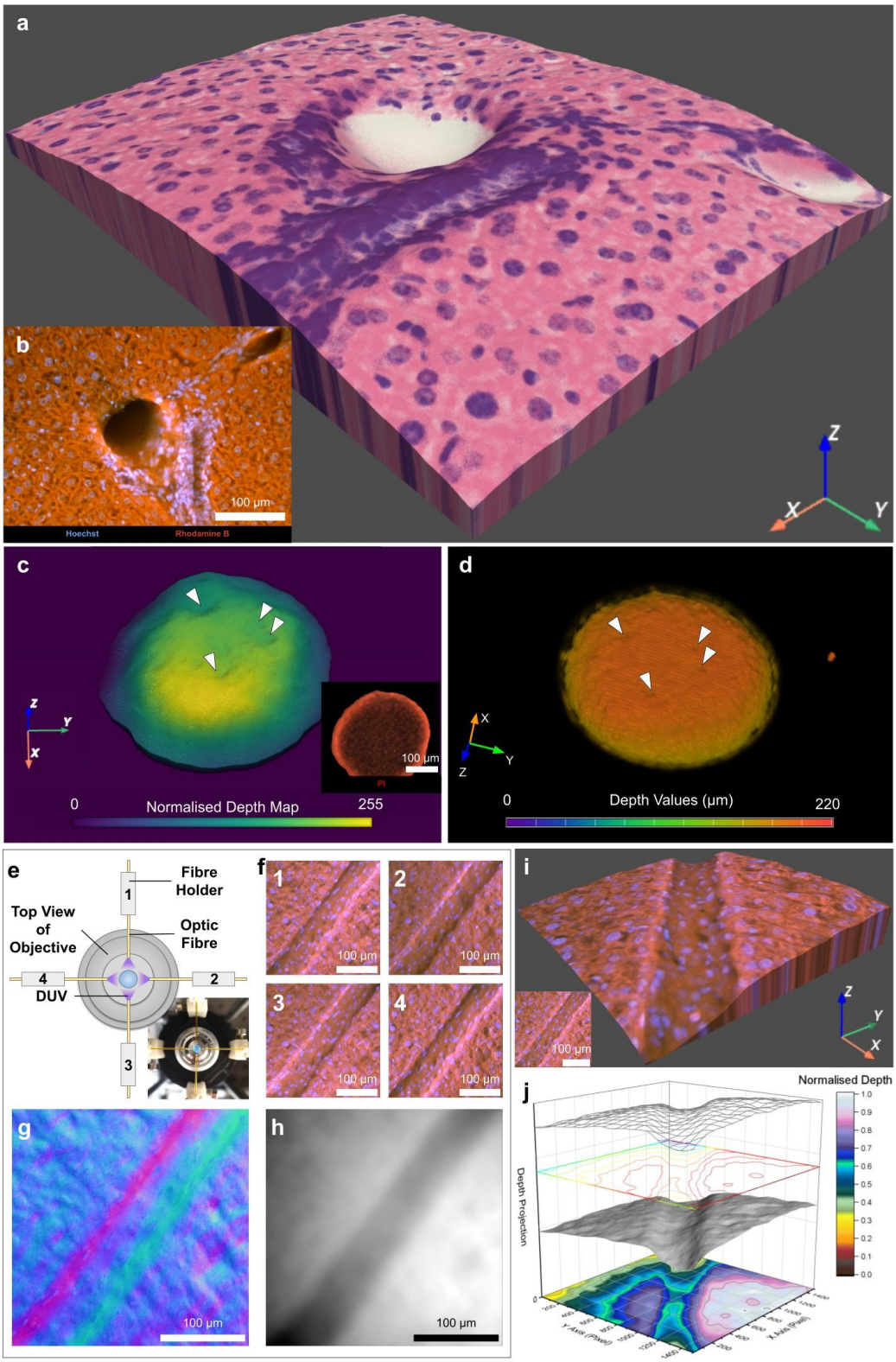

Figure 4: Microtopography. a. 3D virtual H&E recoloured render of fixed mouse liver showing a vein stretching distally into the tissue, with a smaller highly nucleated bile duct running vertically. Further right, a venule, likely feeding to the vein, extends further into the tissue. b. Fluorescence image of the same region-of-interest (blue stain, nucleus stain Hoechst 33342; red-orange stain, counterstain rhodamine B). c. The 3D render presents the normalised depth map of a fixed spheroid (MCF-7) stained with propidium iodide (PI). d. The same spheroid was imaged on a confocal microscope to obtain the depth map of the spheroid. e. Top-down schematic view of the microscope objective showing the fibre arrangement enabling four directions of illumination. f. Images were obtained by sequentially illuminating a longitudinally cut blood vessel in a fixed mouse liver and histogram-matched to a reference image with multi-directional illumination from all four fibres. g. The surface normal vector map is obtained through the photometric stereo algorithm, revealing the liver surface direction, edge and shape of the blood vessel. h. The depth map is obtained from the surface normal map, highlighting the concaved inner wall of the blood vessel. i. 3D render of the blood vessel is shown with the multi-directional illuminated image as the surface texture of the 3D model, allowing a greater appreciation of the 3D physical characteristics of the blood vessel and hepatic surface texture. j. 3D reconstructed normalised depth projection of the region-of-interest is shown, highlighting the 3D depth contours.

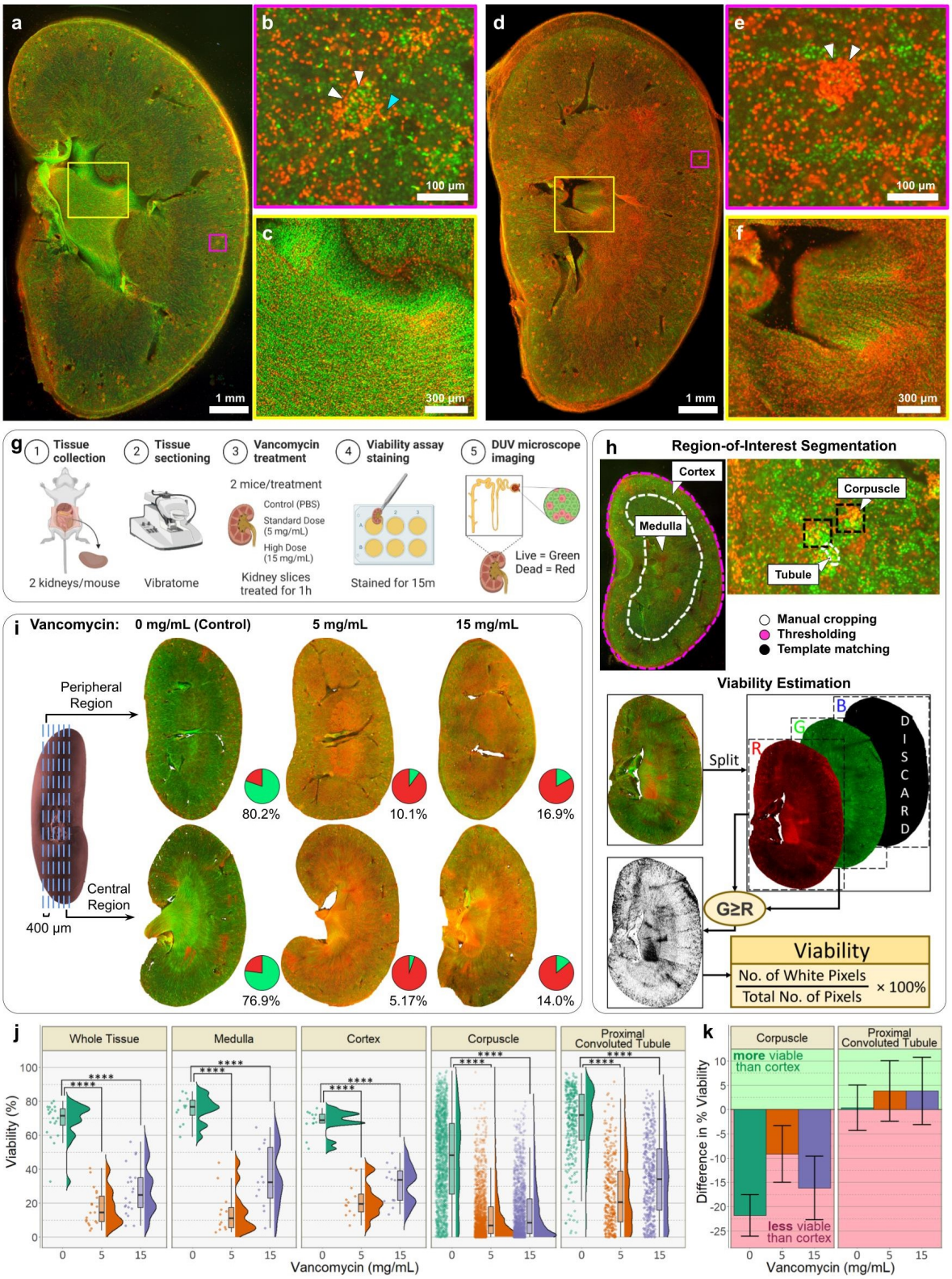

Figure 5: Investigating vancomycin antibiotic effect on *ex vivo* kidney tissue viability. a. Coronal slice of fresh mouse kidney (400 μm-thick) treated with PBS (control) for 1 hour and stained with SYTO 9/propidium iodide (PI). SYTO 9 stains live cells green, PI stains dead cells red. b. Renal corpuscle (white arrowheads) extends to the proximal convoluted tubule (cyan arrowhead) of the kidney nephron. c. Renal calyx differs in structure and staining intensity from surrounding kidney tissue. d. Coronal slice of fresh mouse kidney (400 μm-thick) treated with 5 mg/mL vancomycin for 1 hour and stained with SYTO 9/PI. Vancomycin treatment appears to induce a marked decrease in viability compared to controls. e. Renal corpuscle appears to have lower viability than the surrounding tissue. f. Inner medulla of the kidney (right) transitions to the renal calyx (left). Staining intensity also differs between the calyx and medulla. g. Fresh kidney slices were treated with two concentrations of vancomycin and with PBS as control, before viability assay staining and imaging. h. Segmentation strategies to isolate regions-of-interest for site-specific viability quantitation. Whole kidney slices were segmented from their background using constant thresholding. The medulla and proximal convoluted tubules were manually cropped using ImageJ. Corpuscles were detected using template matching and cropped to a fixed size. Site-specific viability was estimated by comparing the relative intensities of green and red colour channels. i. Kidneys were sliced into five 400 μm-thick slices, which differed in appearance due to the heterogeneous kidney anatomy. Peripheral slices (top row) primarily contained the cortex while central slices (bottom row) also contained the medulla. Pie charts show the estimated viability of the whole kidney slice. j. Distribution of regional estimated viability for each treatment group. There is a statistically significant ($p < 0.0001$) difference in viability with vancomycin treatment regardless of region (whole tissue ($n = 60$), medulla and medulla ($n = 36$), proximal convoluted tubule ($n = 985$), and corpuscles ($n = 4777$). k. Emphasised contrast in the viability of corpuscles and proximal convoluted tubules to their surrounding tissue (the cortex). Error bars denote the T-statistic confidence interval at 0.05 confidence interval.

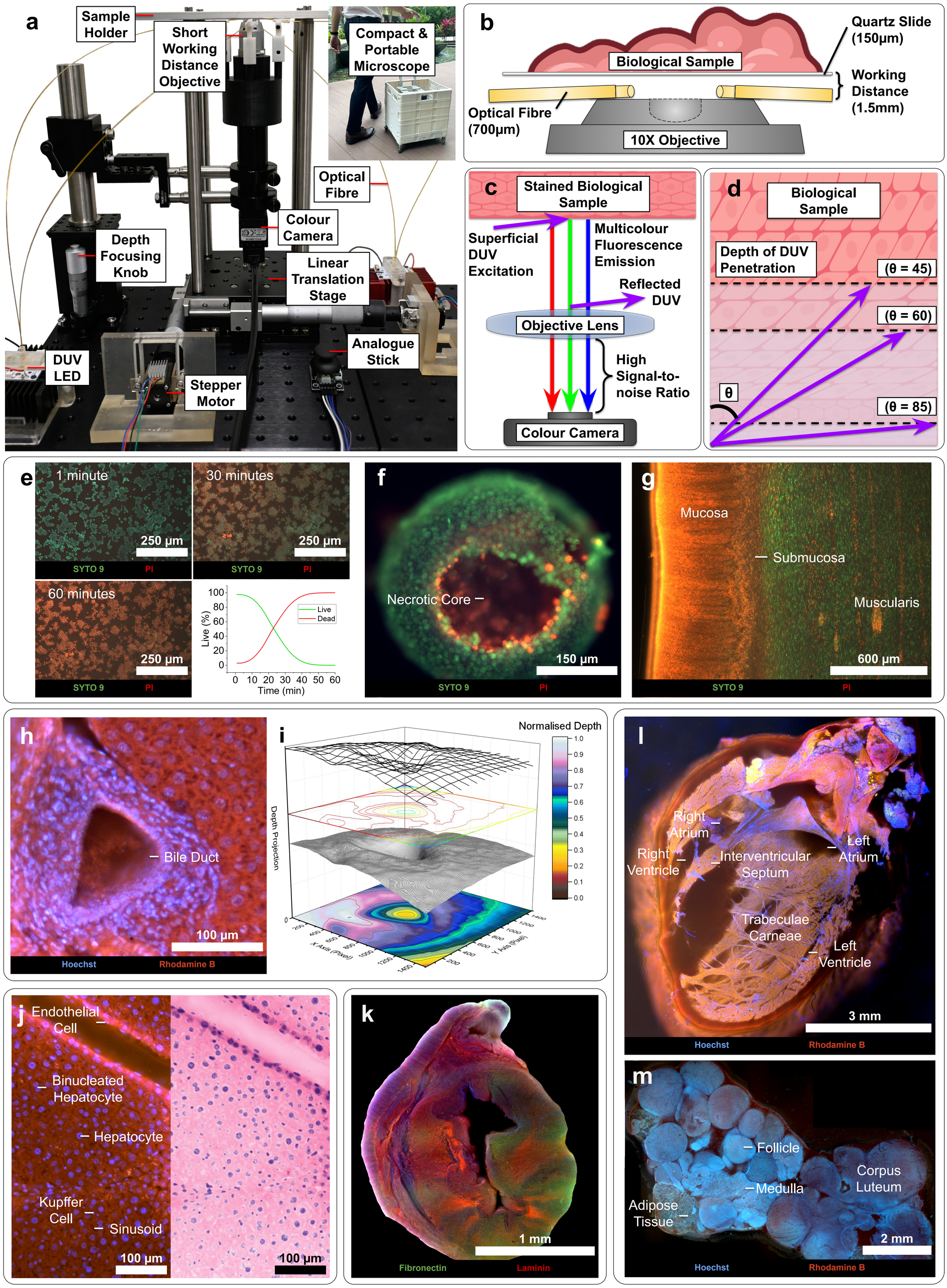
a
Sample Holder
Short Working Distance Objective
Compact & Portable Microscope
Optical Fibre
Colour Camera
Depth Focusing Knob
Linear Translation Stage
Analogue Stick
DUV LED
Stepper Motor
b
Quartz Slide (150µm)
Biological Sample
Working Distance (1.5mm)
Optical Fibre (700µm)
10X Objective
c
Stained Biological Sample
Superficial DUV Excitation
Multicolour Fluorescence Emission
Reflected DUV
Objective Lens
High Signal-to-noise Ratio
Colour Camera
d
Biological Sample
Depth of DUV Penetration
(θ = 45)
(θ = 60)
θ
(θ = 85)
e
1 minute
30 minutes
60 minutes
250 µm
SYTO 9
PI
Live (%)
Time (min)
Live
Dead
f
Necrotic Core
150 µm
g
Mucosa
Submucosa
Muscularis
600 µm
h
Bile Duct
100 µm
Hoechst
Rhodamine B
i
Normalised Depth
Depth Projection
X Axis (Pixel)
Y Axis (Pixel)
l
Right Atrium
Right Ventricle
Interventricular Septum
Left Atrium
Trabeculae Carneae
Left Ventricle
3 mm
Hoechst
Rhodamine B
j
Endothelial Cell
Binucleated Hepatocyte
Hepatocyte
Kupffer Cell
Sinusoid
100 µm
k
1 mm
Fibronectin
Laminin
m
Follicle
Medulla
Corpus Luteum
Adipose Tissue
2 mm
Hoechst
Rhodamine B

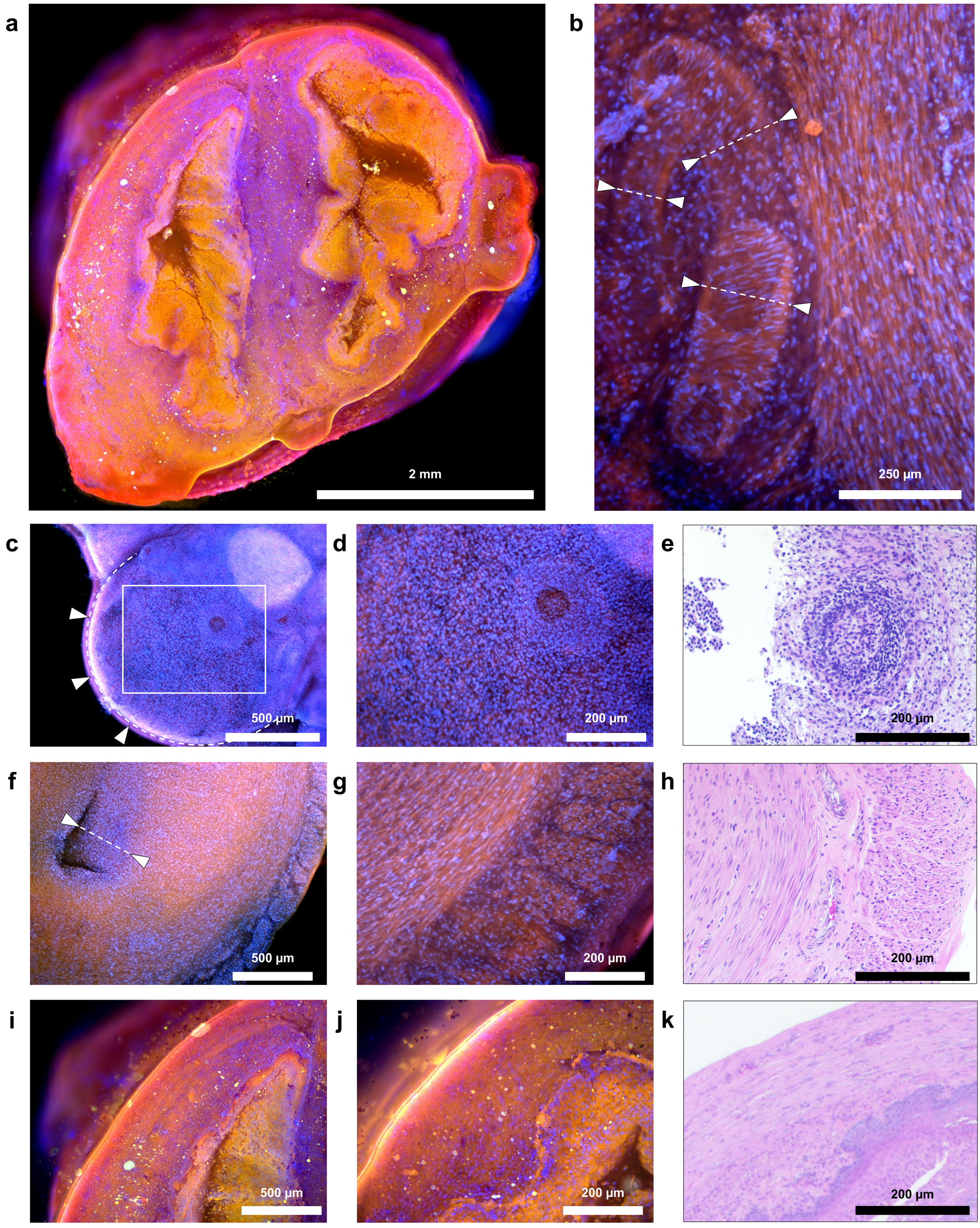
a
2 mm
b
250 µm
c
500 µm
d
200 µm
e
200 µm
f
500 µm
g
200 µm
h
200 µm
i
500 µm
j
200 µm
k
200 µm

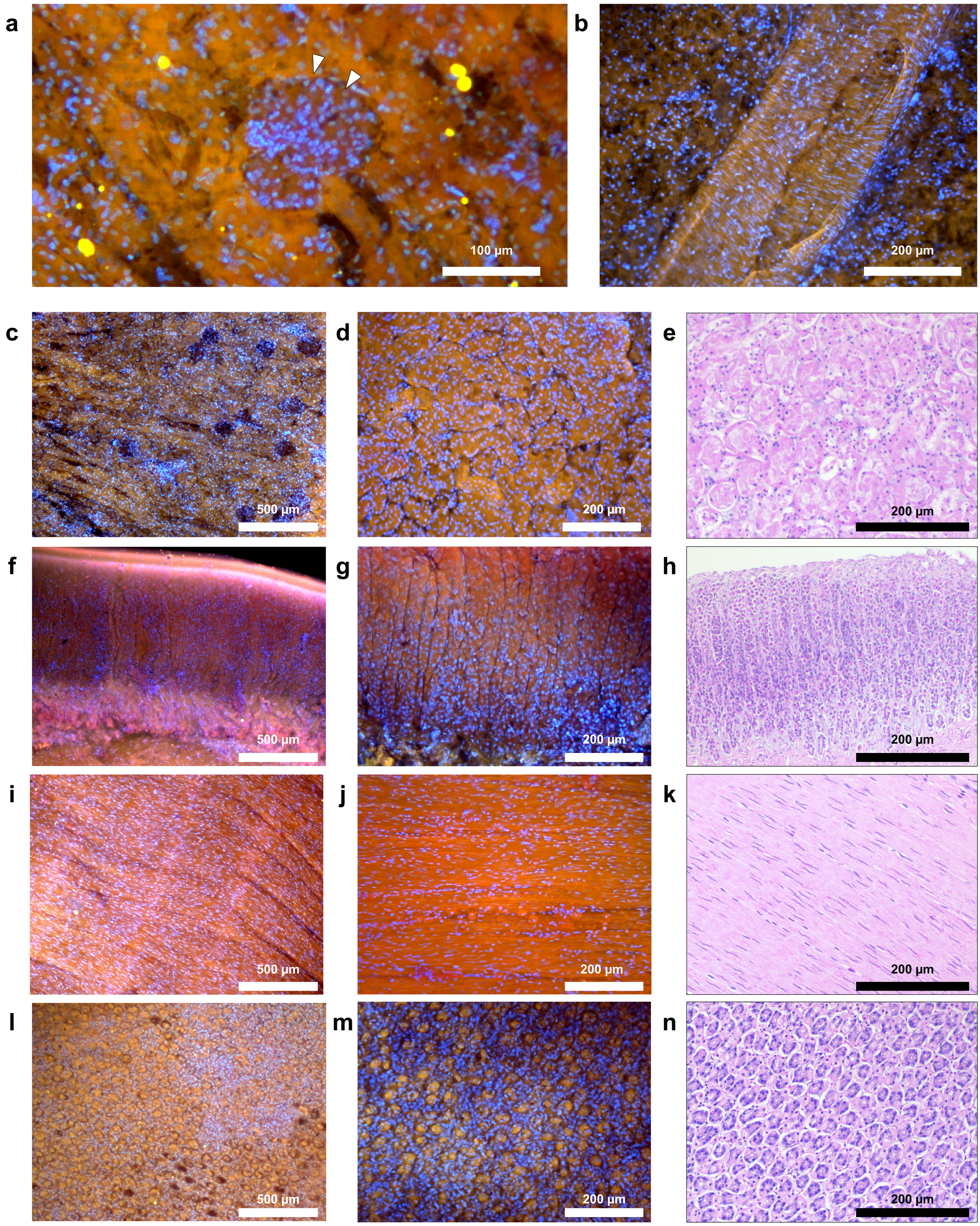
a
100 µm
b
200 µm
c
500 µm
d
200 µm
e
200 µm
f
500 µm
g
200 µm
h
200 µm
i
500 µm
j
200 µm
k
200 µm
l
500 µm
m
200 µm
n
200 µm

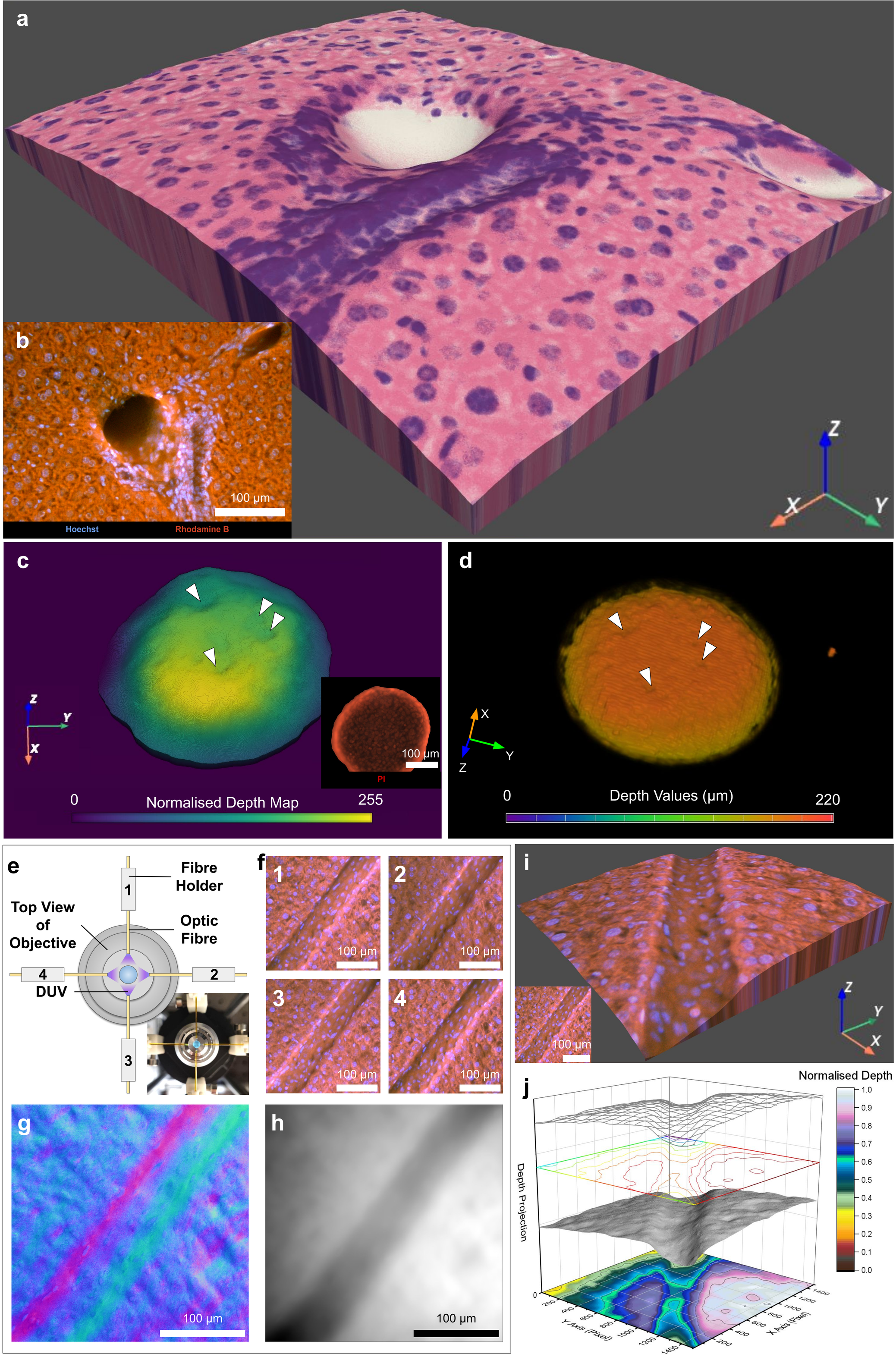
a
b
100 µm
Hoechst
Rhodamine B
Z
X
Y
c
Z
Y
X
100 µm
PI
0
Normalised Depth Map
255
d
X
Y
Z
0
Depth Values (µm)
220
e
Fibre Holder
Top View of Objective
Optic Fibre
1
2
3
4
DUV
f
1
2
3
4
100 µm
g
100 µm
h
100 µm
i
100 µm
Z
Y
X
j
Normalised Depth
1.0
0.9
0.8
0.7
0.6
0.5
0.4
0.3
0.2
0.1
0.0
Depth Projection
0
Y Axis (Pixel)
X Axis (Pixel)
200
400
600
800
1000
1200
1400

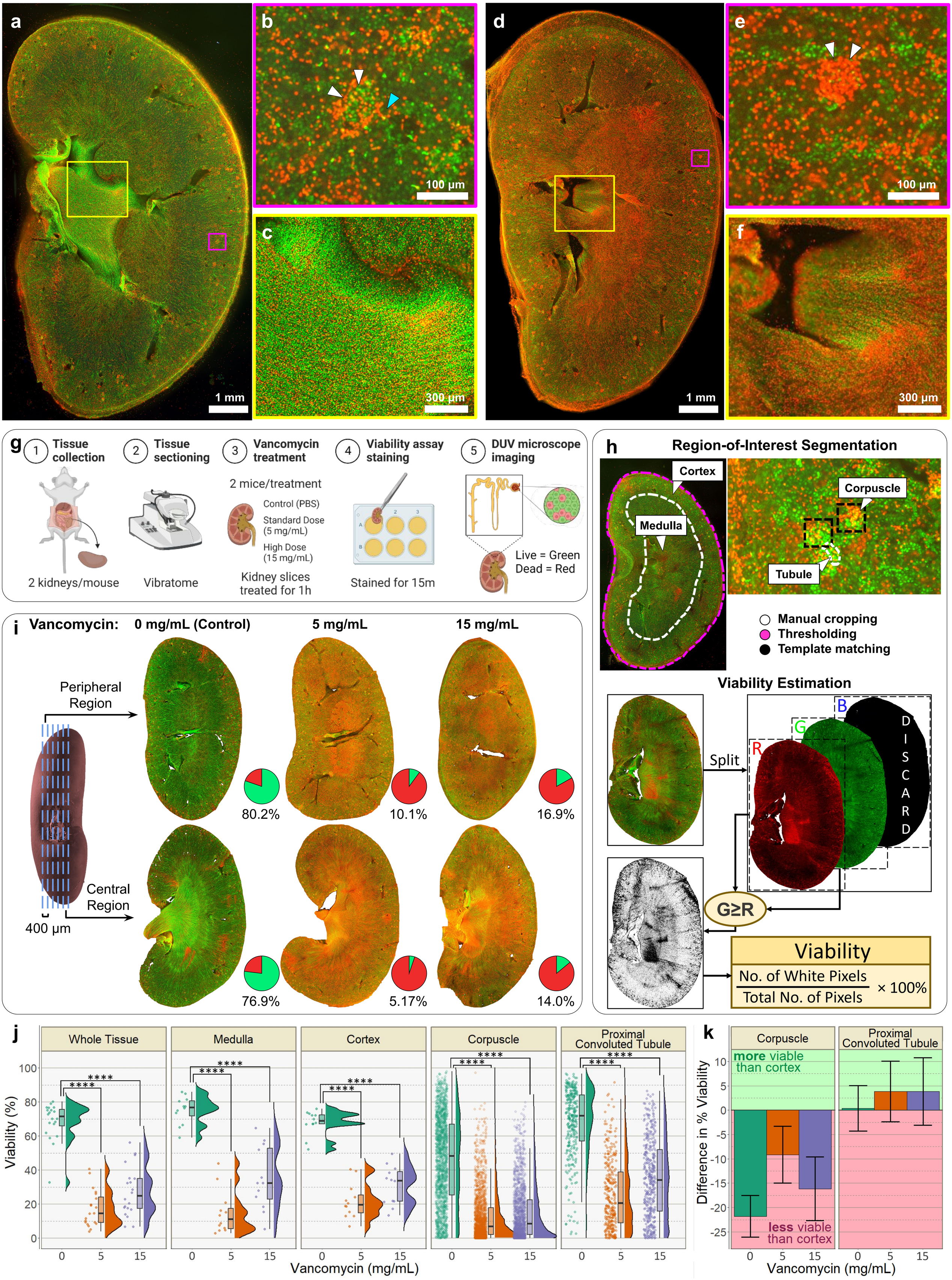
a
b
100 µm
c
300 µm
1 mm
d
e
100 µm
f
300 µm
1 mm
g
1 Tissue collection
2 Tissue sectioning
3 Vancomycin treatment
4 Viability assay staining
5 DUV microscope imaging
2 kidneys/mouse
Vibratome
2 mice/treatment
Control (PBS)
Standard Dose (5 mg/mL)
High Dose (15 mg/mL)
Kidney slices treated for 1h
Stained for 15m
Live = Green
Dead = Red
h
Region-of-Interest Segmentation
Cortex
Medulla
Corpuscle
Tubule
Manual cropping
Thresholding
Template matching
Viability Estimation
Split
B
G
R
DISCARD
G≥R
Viability
No. of White Pixels / Total No. of Pixels × 100%
i
Vancomycin: 0 mg/mL (Control) 5 mg/mL 15 mg/mL
Peripheral Region
Central Region
400 µm
80.2%
10.1%
16.9%
76.9%
5.17%
14.0%
j
Whole Tissue
Medulla
Cortex
Corpuscle
Proximal Convoluted Tubule
Viability (%)
Vancomycin (mg/mL)
k
Corpuscle
Proximal Convoluted Tubule
more viable than cortex
less viable than cortex
Difference in % Viability
Vancomycin (mg/mL)

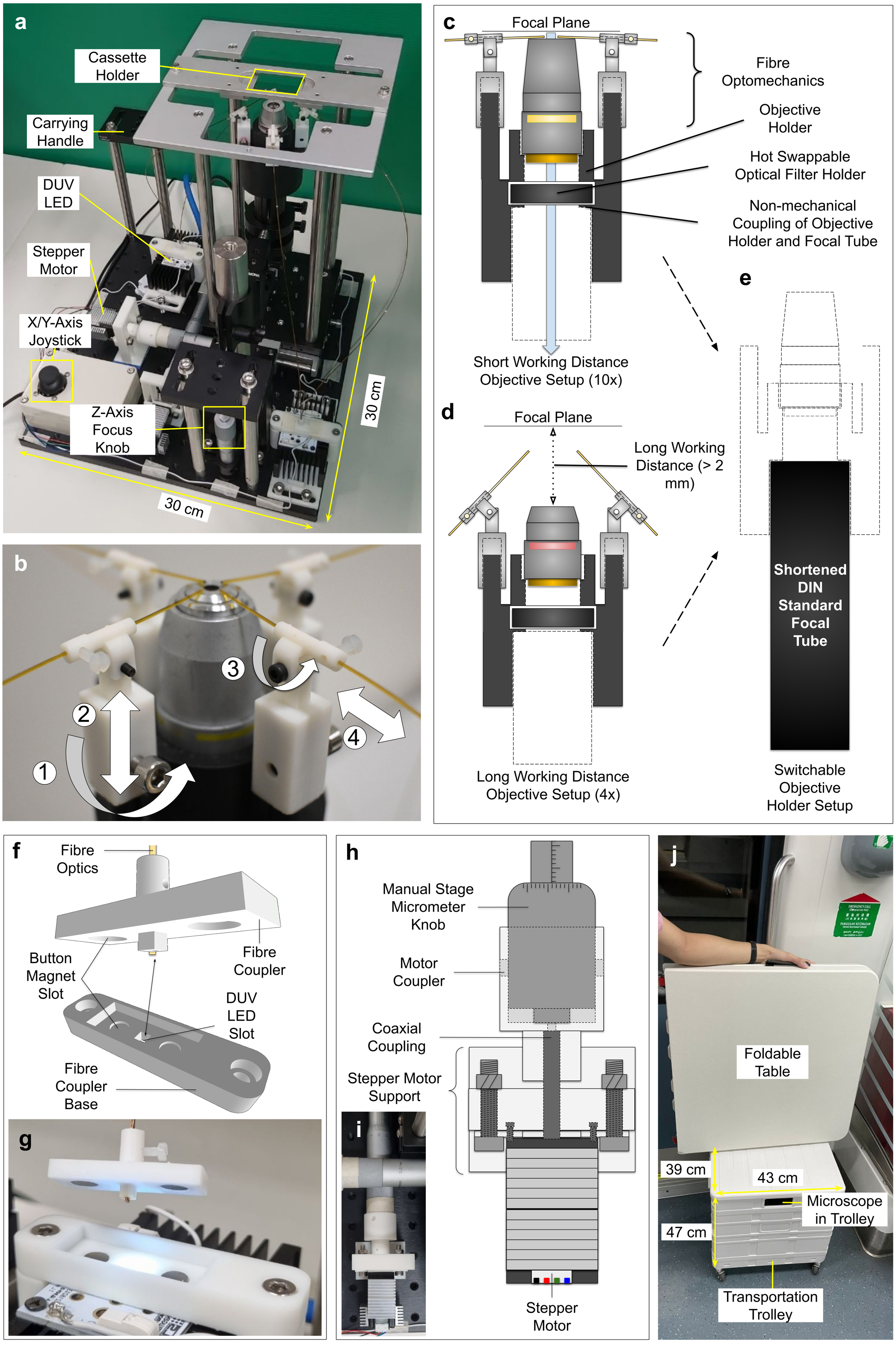
a
Cassette Holder
Carrying Handle
DUV LED
Stepper Motor
X/Y-Axis Joystick
Z-Axis Focus Knob
30 cm
30 cm
b
1
2
3
4
c
Focal Plane
Fibre Optomechanics
Objective Holder
Hot Swappable Optical Filter Holder
Non-mechanical Coupling of Objective Holder and Focal Tube
Short Working Distance Objective Setup (10x)
d
Focal Plane
Long Working Distance (> 2 mm)
Long Working Distance Objective Setup (4x)
e
Shortened DIN Standard Focal Tube
Switchable Objective Holder Setup
f
Fibre Optics
Button Magnet Slot
Fibre Coupler
DUV LED Slot
Fibre Coupler Base
g
h
Manual Stage Micrometer Knob
Motor Coupler
Coaxial Coupling
Stepper Motor Support
Stepper Motor
i
j
Foldable Table
39 cm
43 cm
Microscope in Trolley
47 cm
Transportation Trolley

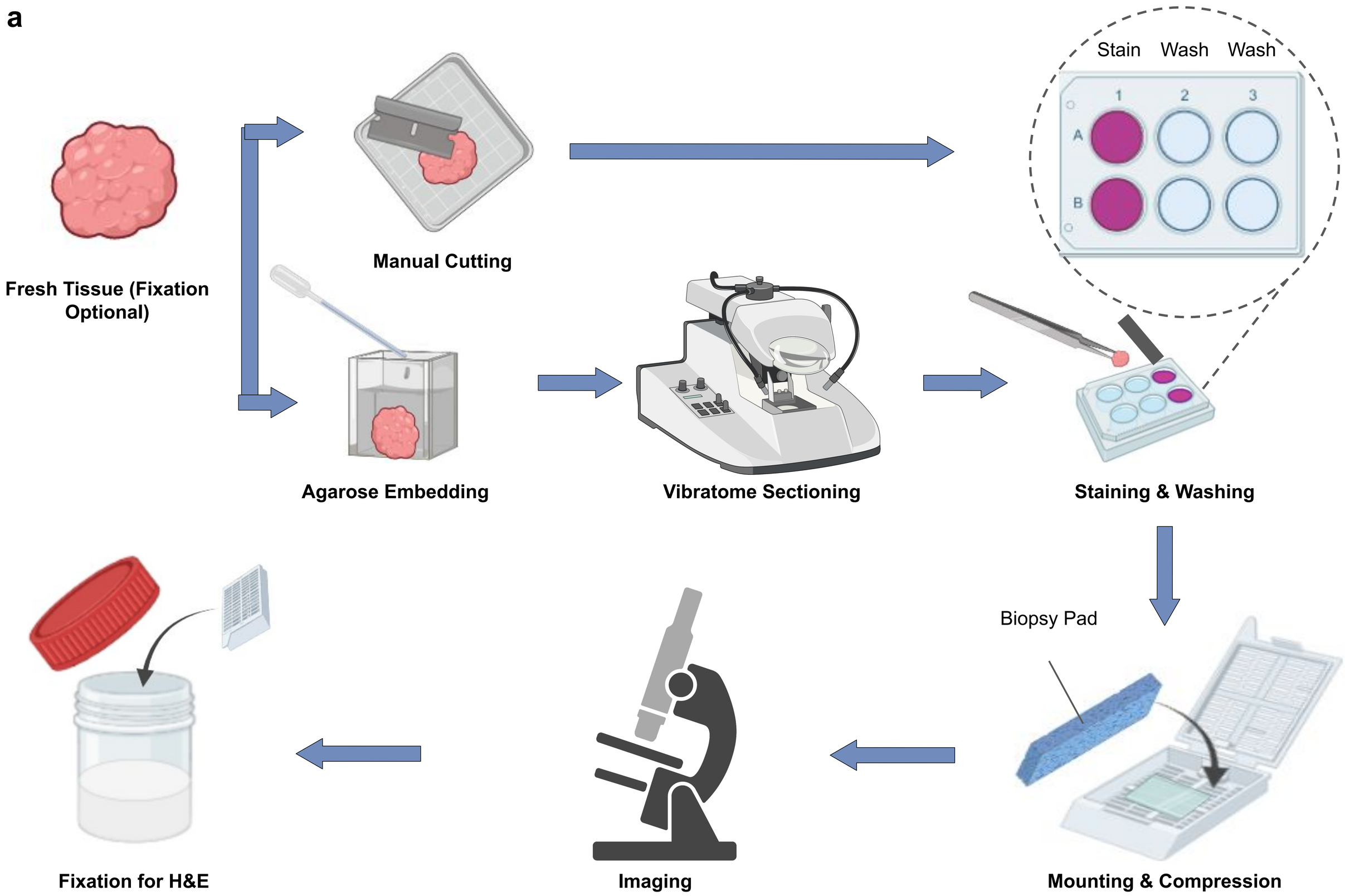
a
Fresh Tissue (Fixation Optional)
Manual Cutting
Agarose Embedding
Vibratome Sectioning
Stain
Wash
Wash
1
2
3
A
B
Staining & Washing
Biopsy Pad
Mounting & Compression
Imaging
Fixation for H&E

b
Surface
Transverse
Array